AGU PUBLICATIONS

Geochemistry, Geophysics, Geosystems

RESEARCH ARTICLE
10.1002/2014GC005576

Key Points:
- We measure the 3-D velocity and temperature fields of a thermal (mantle) plume
- We quantitatively analyze the fluid transport and entrainment of the plume
- We derive and critically discuss a new scaling law for the plume's rise velocity

Supporting Information:
- ms01
- SI_text

Correspondence to:
N. Cagney,
neil.cagney.11@ucl.ac.uk

Citation:
Cagney, N., W. H. Newsome, C. Lithgow-Bertelloni, A. Cotel, S. R. Hart, and J. A. Whitehead (2015), Temperature and velocity measurements of a rising thermal plume, *Geochem. Geophys. Geosyst.*, *16*, 579–599, doi:10.1002/2014GC005576.

Received 19 SEP 2014
Accepted 23 JAN 2015
Accepted article online 30 JAN 2015
Published online 4 MAR 2015

Temperature and velocity measurements of a rising thermal plume

Neil Cagney[1], William H. Newsome[2], Carolina Lithgow-Bertelloni[1], Aline Cotel[3], Stanley R. Hart[4], and John A. Whitehead[5]

[1]Department of Earth Sciences, University College London, London, UK, [2]Department of Geological Sciences, University of Michigan, Ann Arbor, Michigan, USA, [3]Department of Civil and Environmental Engineering, University of Michigan, Ann Arbor, Michigan, USA, [4]Geology and Geophysics Department, Woods Hole Oceanographic Institute, Woods Hole, Massachusetts, USA, [5]Physical Oceanography Department, Woods Hole Oceanographic Institute, Woods Hole, Massachusetts, USA

Abstract The three-dimensional velocity and temperature fields surrounding an isolated thermal plume in a fluid with temperature-dependent viscosity are measured using Particle-Image Velocimetry and thermochromatic liquid crystals, respectively. The experimental conditions are relevant to a plume rising through the mantle. It is shown that while the velocity and the isotherm surrounding the plume can be used to visualize the plume, they do not reveal the finer details of its structure. However, by computing the Finite-Time Lyapunov Exponent fields from the velocity measurements, the material lines of the flow can be found, which clearly identify the shape of the plume head and characterize the behavior of the flow along the plume stem. It is shown that the vast majority of the material in the plume head has undergone significant stretching and originates from a wide region very low in the fluid domain, which is proposed as a contributing factor to the small-scale isotopic variability observed in ocean-island basalt regions. Lastly, the Finite-Time Lyapunov Exponent fields are used to calculate the steady state rise velocity of the thermal plume, which is found to scale linearly with the Rayleigh number, in contrast to some previous work. The possible cause and the significance of these conflicting results are discussed, and it is suggested that the scaling relationship may be affected by the temperature-dependence of the fluid viscosity in the current work.

1. Introduction

Mantle plumes are columns of hot, buoyant material rising from deep in the mantle to the lithosphere, and are thought to be the cause of various "hot spots," Ocean Island Basalts (OIBs) and the formation of large igneous provinces [*Morgan*, 1971; *Campbell and Griffiths*, 1990]. These volcanic features have a varied isotopic signature that is distinct from that of mid-ocean ridge basalts (MORBs), which are derived from the upper layers of the mantle [*Zindler and Hart*, 1986; *Hofmann*, 1997; *White*, 2010; *Hawkesworth and Scherstén*, 2007]. These differences in the isotopic characteristics have been explained in terms of the ability of the plume to raise material from very deep in the mantle, often the core-mantle boundary (CMB) [*Morgan*, 1971], to entrain material from the mid-mantle [*Griffiths and Campbell*, 1990; *Hart et al*., 1992; *Lin and van Keken*, 2006] and/or to bring material from the 660 km discontinuity [*Cserepes and Yuen*, 2000].

The behavior of thermal plumes are controlled by the nondimensional Rayleigh number,

$$\mathrm{Ra} = \frac{\rho \alpha \Delta T g D^3}{\mu \kappa}, \tag{1}$$

where ρ is the density of the ambient fluid, α is the thermal expansion coefficient, ΔT is the temperature difference across the fluid, g the acceleration due to gravity, D is the depth of the fluid domain, and μ and κ are the dynamic viscosity and thermal diffusivity of the fluid, respectively. This is essentially the ratio of the buoyancy forces to the effects of viscous and thermal dissipation. Alternatively, the Rayleigh number can be defined in terms of the heat flux density into the fluid domain, q'',

$$\mathrm{Ra}_Q = \frac{\rho \alpha q'' g D^4}{\mu \kappa k}, \tag{2}$$

where k is the thermal conductivity of the fluid.

The dynamics of the plumes is also controlled by the Prandtl number of the fluid, $\mathrm{Pr}=\nu/\kappa$ (where $\nu=\mu/\rho$), which is the ratio of the viscous to thermal dissipation, and is thought to be $\sim 10^{23}$ in the mantle. The Rayleigh number is also thought to be very large $(\mathrm{Ra} \sim 10^7)$, implying that several plumes are present and the mantle undergoes vigorous stirring over geological time scales.

The behavior of plumes in the mantle is likely to be complicated by effects such as the depth dependence of material properties, non-Newtonian viscosity and phase changes. Various researchers have attempted to model some of these complex features experimentally [*Kumagai and Kurita*, 2000; *Kumagai et al*., 2007] and numerically [*van Keken*, 1997; *Farnetani et al*., 2002; *Farnetani and Samuel*, 2005; *Lin and van Keken*, 2006; *Li et al*., 2014]. However, the behavior of isolated plumes in a fluid with isotropic, Newtonian properties is still not well understood. For example, various alternate scaling relationships have been proposed for the rise velocity of plumes [*Batchelor*, 1954; *Whitehead and Luther*, 1975; *Griffiths and Campbell*, 1990; *Moses et al*., 1993]. This may in part be because several studies have examined plumes generated by the injection of buoyant fluid [e.g., *Olson and Singer*, 1985; *Griffiths and Campbell*, 1990; *Rogers and Morris*, 1990; *Bercovici and Mahoney*, 1994], rather than those generated by a heater (which is closer to the nature of the heating in the mantle). The use of injection systems creates an additional controlling variable, the volume flow rate, and the difference in the source of buoyancy is likely to have a significant effect on the fluid dynamics.

Many of the laboratory experiments investigating thermally generated plumes have been qualitative in nature (with some notable recent exceptions, e.g., *Davaille et al*. [2005], *Kumagai et al*. [2007], *Limare et al*. [2008], *Vatteville et al*. [2009], and *Davaille et al*. [2011]), typically visualizing the temperature field surrounding plumes using shadowgraphs [*Schlien*, 1976; *Moses et al*., 1993] or interferometry [*Chay and Schlien*, 1986; *Kaminski and Jaupart*, 2003]. However, such qualitative measurements of the temperature field do not give direct information on the flow field, and are not guaranteed to be directly comparable to flow visualization work, regardless of the manner in which the plume was created. As a result, there is no generally accepted means by which to define the position or geometry of a plume.

The aim of this paper is to present quantitative, three-dimensional measurements of the velocity and temperature fields of an isolated thermal plume in a fluid with temperature-dependent viscosity, and to provide a means to define the plume position. The fluid is otherwise homogeneous, and we ignore any potential effects of phase-changes or depth-dependent fluid properties. The remainder of the paper is structured as follows; the experimental system used to generate and characterize the thermal plume is described in section 2; the velocity and temperature fields are presented in section 3.1; section 3.2 describes the flow field and plume geometry in terms of the Lagrangian flow structures; section 3.3 discusses the paths of fluid elements through the flow and the entrainment of ambient material; a discussion of the scaling laws associated with the rise velocity is presented in section 3.4; and lastly some concluding remarks are made in section 4.

2. Experimental Details

The experiments were performed in a cubic test section with 10 mm thick acrylic walls, and internal dimensions of 265 mm, which is shown schematically in Figure 1. A circular heater with a diameter of 20 mm was installed at the center of the test section, flush with the lower surface. The heater was connected to a programmable closed-loop controller and monitored using a thermocouple.

The origin of the reference frame was fixed at the center of the heater, as shown in Figure 1, with y measured in the vertical direction from the bottom of the tank.

The working fluid was corn syrup (LSI Specialty Products' Liquidose 436), which is known to have a Newtonian but highly temperature-dependent viscosity. Some of the properties of the fluid at 25°C are listed in Table 1. The syrup viscosity was measured in the laboratory for the temperature range 24°C–90°C, as shown in Figure 2, and was found to vary with temperature according to

$$\mu = 1080 e^{-0.156T + 6.25\times10^{-4}T^2}\,(\mathrm{Pa.s}), \tag{3}$$

where T is temperature, measured in degrees Celsius.

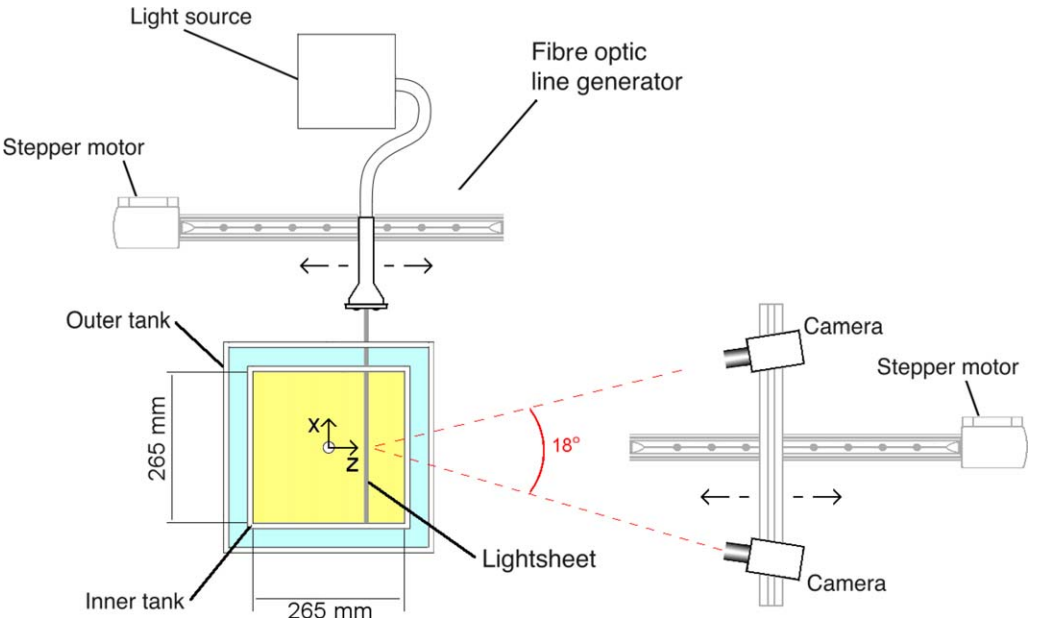

Figure 1. Schematic showing the test section and measurement and coordinate systems used. The light source and the cameras were mounted on movable traverse systems. The yellow region in the test section shows the syrup, while the surrounding blue region is the outer tank, containing water.

The test section was enclosed in an outer tank, in which water was held constant at 25.2°C. Four experiments were performed in which the heater temperature was held at $\Delta T = 24.9$°C, 34.8°C, 44.9°C, and 54.9°C, where ΔT is the temperature difference between the heater and the ambient temperature. Figure 3 shows the time histories of the heater temperature for each of the four experiments; after a brief overshoot, the heater temperature was found to be constant to within ± 0.25°C. This corresponds to a Rayleigh number range of 0.62–1.37 $\times$ 10^6, and maximum viscosity contrasts of $\gamma = \mu/\mu_{min} = 15-142$ (equation (3)). In each case, the velocity and temperature fields were measured throughout the test section, as outlined in the following subsections.

2.1. Velocity Measurements

The three-dimensional velocity fields were measured using scanning stereoscopic Particle-Image Velocimetry (PIV), which is a standard technique in experimental fluid mechanics. The method relies on taking pairs of images (separated by a time-lag, Δt) of an illuminated measurement plane, and using image processing to estimate the displacement, $\Delta \mathbf{x}$, of each region of fluid. The velocity field can be estimated by $\mathbf{u} = \Delta \mathbf{x}/\Delta t$. See *Raffel et al*. [2007], *Adrian and Westerweel* [2011], and *Westerweel et al*. [2013] for a complete description of the method.

The measurement plane was illuminated using a halogen white light source and a fiber optic line generator. Two CCD cameras separated by 18° were used to image the plane, as shown in Figure 1. The flow was uniformly seeded with high-gloss, white polymer powder, which had a variable diameter in the range 1–40 μm, as well as the thermochromatic liquid crystals, which will be discussed in the following section.

Table 1. Corn Syrup Properties at 25°C[a]

Property	Symbol	Value
Density	ρ	1439 kg/m^3
Dynamic viscosity	μ	32.3 Pa.s
Kinematic viscosity	ν	0.022 m^2/s
Thermal expansion coefficient	α	3.1×10^{-4} K^{-1}
Specific heat capacity	C_p	2280 J/kg.K
Thermal diffusivity	κ	1.04×10^{-7} m^2/s
Prandtl number	Pr	2.15×10^5

[a]The specific heat capacity and thermal diffusivity were provided by the manufacturer, while all other properties were measured in the laboratory.

The cameras and the light sheet were mounted on traverse systems which could be moved independently (see Figure 1), such that PIV measurements could be acquired throughout the span of the test section, at increments of $z = 5$ mm. For each experiment, the velocity fields

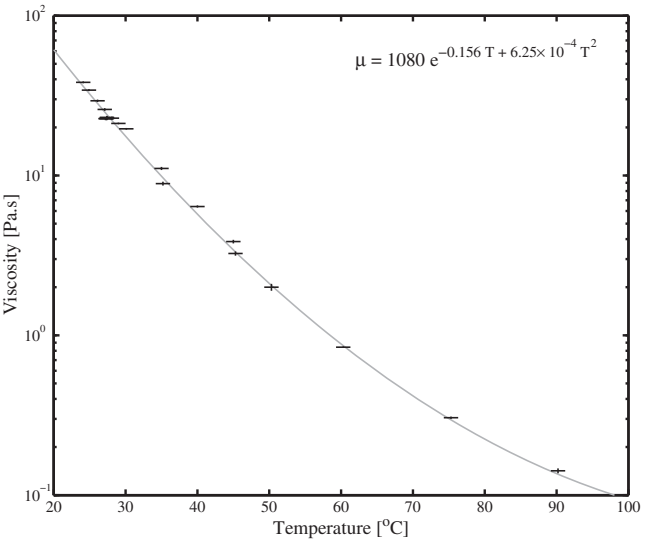

Figure 2. Variation in the measured viscosity of the working syrup with temperature (black crosses) and the best fit exponential relationship (gray line, equation (3)). The lines in each symbol represent the uncertainties, which were in the range ±0.005–0.5 Pa s for viscosity, and ±1°C for temperature. The best fit line had an R^2 value of 0.99.

throughout the tank were estimated at 39 time steps, spanning the time at which the heater was turned on until the plume neared the upper top of the tank. Because of the finite time required to move the cameras and the light sheet, the velocity fields at each plane for each time step could not be acquired at exactly the same instant. In order to account for this, the planar measurements were linearly interpolated forward in time, so that they all corresponded to the time at which the last plane at each time step was acquired. The final time step of each experiment could not be synchronized in this manner (but could be used to synchronized the penultimate time step) and was discarded. Thus, for each experiment, 38 synchronized three-dimensional velocity fields were acquired.

The velocity fields for each camera were estimated using in-house code [*Newsome*, 2011]. A two-pass scheme was employed, which had a final vector spacing of 16 × 16 pixels. The final velocity fields had a resolution of 2.79 mm in the *x* and *y* directions.

The errors associated with PIV are typically less than half a pixel divided by Δt [*Raffel et al.*, 2007]. It is therefore beneficial to choose large values of Δt, where possible; in this case, the magnitude of the displacements of the fluid regions between frames is larger and the relative error in the velocity fields is reduced. However, the use of large $\Delta \mathbf{x}$ incurs a significant computational burden. To compensate for this, the Sequential Similarity Detection Algorithm of *Barnea and Silverman* [1972] was used for the first pass, while the (slower) normalized cross-correlation method was used for the second pass. Visual inspection of sample velocity fields did not reveal any noticeable loss of accuracy compared to the use of normalized cross correlation for both passes.

In some cases, spurious or erratic PIV vectors were observed near the base of the heater due to the high local shear. PIV vectors for which the normalized cross-correlation coefficient, N_C, was less than 0.7 (N_C is a representation of the correlation between two windows, and occurs between −1 and 1) were reprocessed using Particle-Tracking Velocimetry (PTV), which is insensitive to local velocity gradients [*Cowen and Monismith*, 1997; *Adrian and Westerweel*, 2011]. The motion of each particle in the window was tracked and the velocity was averaged to find the replacement vector. The details of the implementation of the tracking method can be found in *Newsome* [2011].

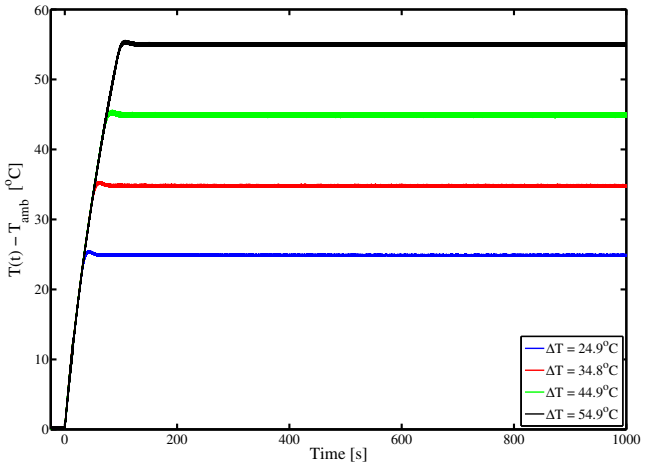

Figure 3. Time histories of the heater temperature for each experiment.

Following each pass, the velocity fields in each plane were processed

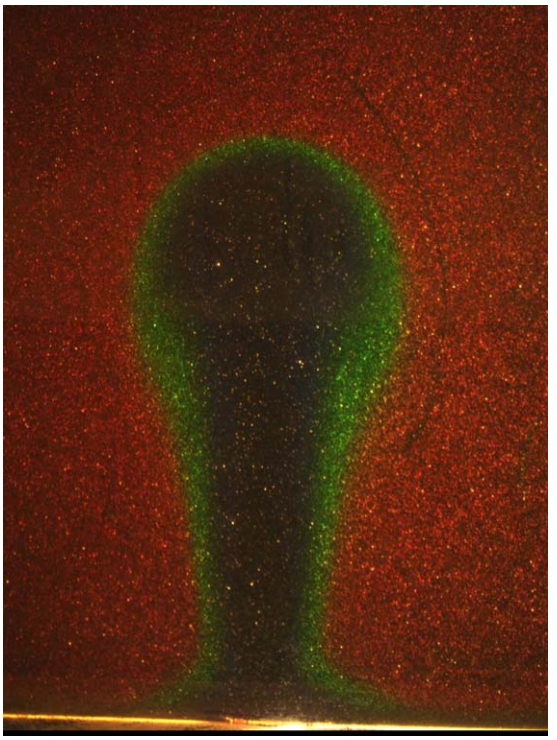

Figure 4. A sample image, showing the PIV tracers (white particles) and TLCs (colored particles). The heater is at the bottom center of the image, and the dark region represents the rising thermal plume. The red regions indicates the colder regions of the fluid, where the temperature is approximately 25.2°C, while the dark areas correspond to regions where the temperature is above the color-play range, i.e., >26.8°C. The white particles scattered throughout the entire images are the passive tracers used for PIV.

using the normalized median filter test of *Westerweel and Scarano* [2005] and smoothed using a Gaussian filter. The fields from each camera were combined to provide the third velocity component [*Willert*, 1997], and the final three-dimensional velocity fields were again processed using a three-dimensional normalized median test and smoothing filter. The final three-dimensional vector fields spanned a region, $x = -78$ to 86.4 mm, $y = 1.39$ to 215.9 mm, and $z = -132.5$ to 132.5 mm. Standard PIV is not effective at measuring the fluid velocity very close to solid boundaries [*Nguyen et al*., 2010]; therefore, it was not possible in the current system to measure the flow within 1.39 mm (i.e., half a vector spacing) of the lower surface of the tank.

The PIV measurements may underestimate the maximum velocity in the plume stem for a number of reasons; first, as well as reducing noise, the various smoothing operations will also decrease local velocity maxima, and second, PIV produces an inherently low-pass estimate of the velocity field (since each vector represents the average velocity in a given window). These factors may act to reduce the magnitude of the vertical velocity measured along the plume stem, $v_{max,0}$.

In order to quantify this effect, the velocity along the plume axis was measured using PTV only (which is unaffected by velocity gradients). No smoothing was applied to the final PTV estimates, and each velocity vector was found using the *largest* particle displacement in the window (rather than the average). This will lead to a slight *overestimation* of $v_{max,0}$ since the tracking of individual tracers tends to be less accurate than the tracking of groups of particles, as in PIV. The values of $v_{max,0}$ found using the standard PIV approach used throughout these experiments were on average 6.3% lower than the estimates found using PTV alone. This value was taken to represent an upper bound on the uncertainty of the velocity measurements.

2.2. Temperature Measurements

Thermochromic Liquid Crystals (TLCs) provide a quantitative, noninvasive means to measure the temperature field throughout a fluid. The wavelength of the light scattered by the TLCs depends on the temperature and viewing angle [*Fergason*, 1968; *Raynes*, 1983]. Within a certain range of temperature known as the color-play, the crystals emit light in the visible spectrum, which can be captured by the CCD cameras, and can thus be used to calculate the temperature. See *Dabiri* [2009] for a full description of the technique and calibration process.

The TLCs used in the current work were manufactured by LCR Hallcrest (Formulation NSL33R25C15W100), were 50–100 μm in diameter, and in the sugar syrup, were found to have a color-play of 25.2–26.8°C. This provided the motivation to set the ambient temperature to be 25.2°C. A sample PIV image showing the TLCs is presented in Figure 4. The red regions indicate the areas where the temperature is approximately 25.2°C. Near the center of the plume, the fluid is hotter, the temperature is outside the color-play, and the crystals are essentially transparent.

The TLCs were calibrated throughout the tank by increasing the ambient temperature in increments of 0.2°C (in the absence of any plumes). Each PIV image acquired by the right camera in Figure 1 was

processed to estimate the temperature field. The images were decomposed into blocks before processing such that the final estimates had the same spatial resolution as the velocity fields (i.e., 16 × 16 pixels or 2.79 × 2.79 mm). The fields were also synchronized and processed using the normalized median test and Gaussian smoothing, in the same manner as the velocity fields.

The temperature measurements are strongly influenced by the refractive index of the working fluid, which is inherently accounted for in the calibration process. However, as the fluid is heated at a point, the refractive index will also change locally, potentially making the temperature measurements inaccurate in certain regions. In practice, this meant that the refractive index changes within the plume made the measurements inside the plume unreliable. As a result, it was decided to only use the temperature measurements to identify the 25.25°C isotherm. This is only 0.05°C above the ambient temperature, and can be used to identify the approximate thermal boundary of the plume, as will be shown in Figures 5–7.

2.3. Lagrangian Coherent Stuctures

Velocity measurements are typically performed in an Eulerian reference frame, i.e., one which is fixed in space. However, it is often possible to extract important information about a flow using analysis performed in a Lagrangian frame, i.e., one which moves with the fluid. In particular, it is possible to identify the Lagrangian Coherent Structures (LCSs), or "material lines" of the flow (material *surfaces* in the case of three-dimensional flow). These are lines in the flow across which no fluid passes, and which separate qualitatively distinct regions of the flow [*Shadden et al*., 2005; *Mathur et al*., 2007]. LCSs can be classed as *attracting* or *repelling*, depending on whether the local fluid particles tend to advect toward or away from them. Several researchers have applied Lagrangian analysis to numerical simulations [*Farnetani and Richards*, 1995; *Farnetani et al*., 2002; *Lin and van Keken*, 2006], although there has been little work which has applied this methodology to experimental data relevant to geophysics.

The velocity measurements produced by PIV are fixed in an Eulerian reference frame. In order to perform Lagrangian analysis, it is typical to numerically advect passive tracers (with zero size and mass) through the measured velocity fields using some variant of the Runge-Kutta scheme [*Ferziger*, 1998]. The LCSs can be identified from ridges in the Finite-Time Lyapunov Exponent (FTLE) field, $\sigma_f(\mathbf{x}, t)$. This is a measure of the maximum exponential rate at which neighboring particles at a point $\mathbf{x}$ will separate over some integration time, τ. It is defined as

$$\sigma_f(\mathbf{x}, t) = \frac{1}{|\tau|} \log\left(\frac{\max(\|\delta\mathbf{x}(t)\|)}{\max(\|\delta\mathbf{x}(t_0)\|)}\right), \tag{4}$$

where t_0 is the time at which the tracer advection began (typically the start of the experiment), $\max(\|\delta\mathbf{x}(t)\|)$ is the maximum separation between neighboring tracers at time t, and $\tau = t - t_0$. Typically, the tracers are uniformly distributed with some spacing Δx_0 at t_0, in which case the denominator is given by $\max(\|\delta\mathbf{x}(t_0)\|) = \Delta x_0$.

The FTLE fields can also be computed in backward-time, by reversing the velocity and choosing $t < t_0$. Ridges in the backward-time σ_f fields tend to correspond to attracting material lines, while those in forward time tend to correspond to repelling lines. However, in practice, the topology of the σ_f fields must be examined to ensure that the various ridges are representative of true material lines, and are not merely a consequence of the numerical implementation (i.e., the finite time or finite measurement domain in experimental studies). See *Shadden et al*. [2005] and *Haller* [2015] for a detailed description of the computation and use of FTLE fields.

The FTLE fields are representative of the magnitude of the separation of local tracers over the interval $t_0 - t$ in forward or backward-time; therefore, the regions of high or low FTLE represent regions of strong or weak fluid stretching, respectively, which is useful in the analysis of mixing within flows.

Except where otherwise stated, the Lagrangian analysis was performed by numerically advecting tracers through the velocity fields acquired in the center-plane of the test section. At the initial time, t_0, the tracers were uniformly distributed throughout the PIV domain, with a spatial resolution three times greater than that of the velocity vectors (i.e., a resolution of 0.93 × 0.93 mm). A fourth-order Runge-Kutta scheme with cubic interpolation in time and space was used to advect the tracers. For the forward-time computations, the tracers were advected from the start of the experiment ($t = 0$) until the current time, t, while for the

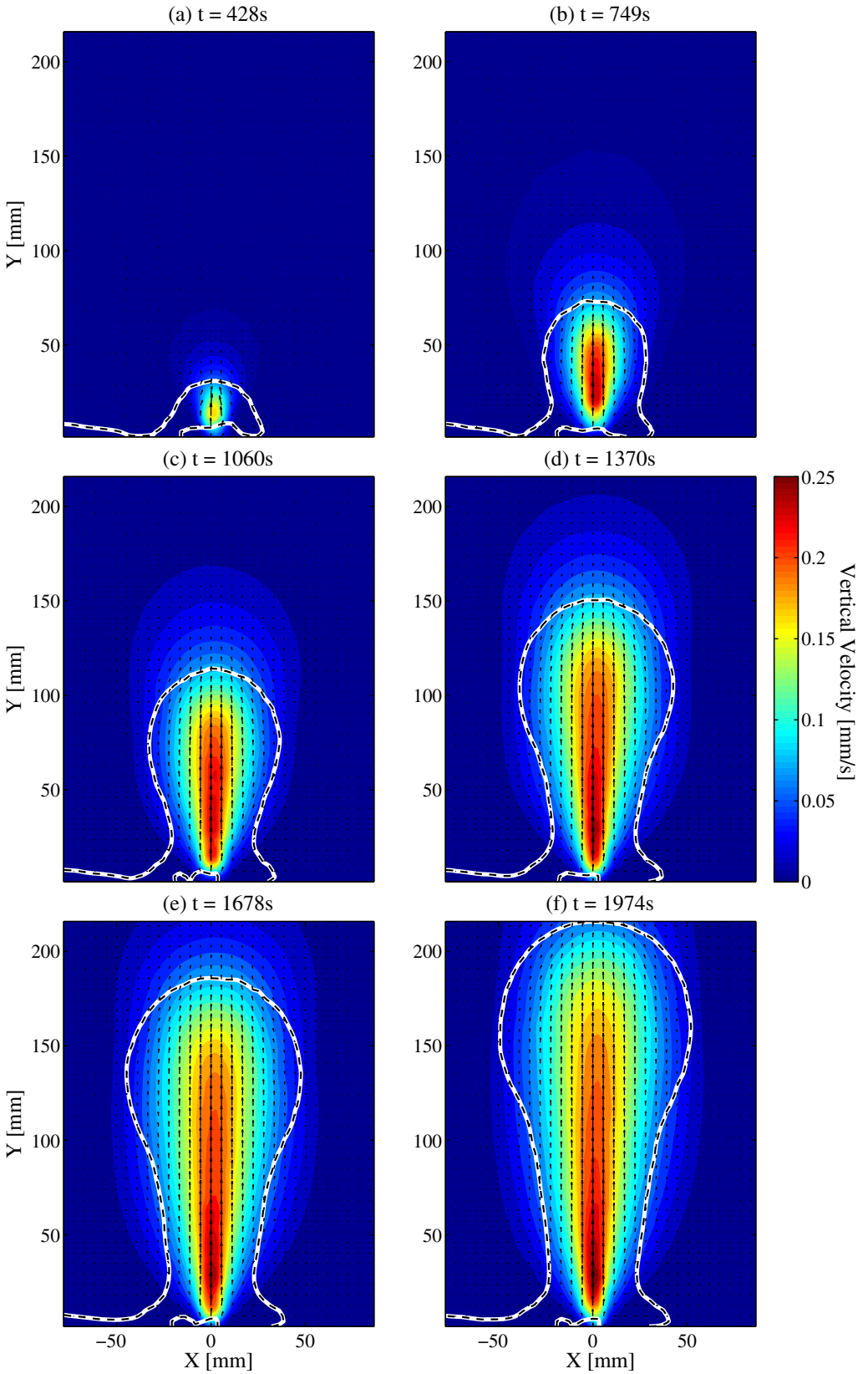

Figure 5. Contours of the vertical component of the velocity field, and the 25.25°C ($\Delta T = 0.05$°C) isotherm (white lines) measured at the center-plane ($z = 0$) at six instances for Ra = 1.37×10^6. The vector field is also overlaid (for clarity only every second vector in either direction is shown).

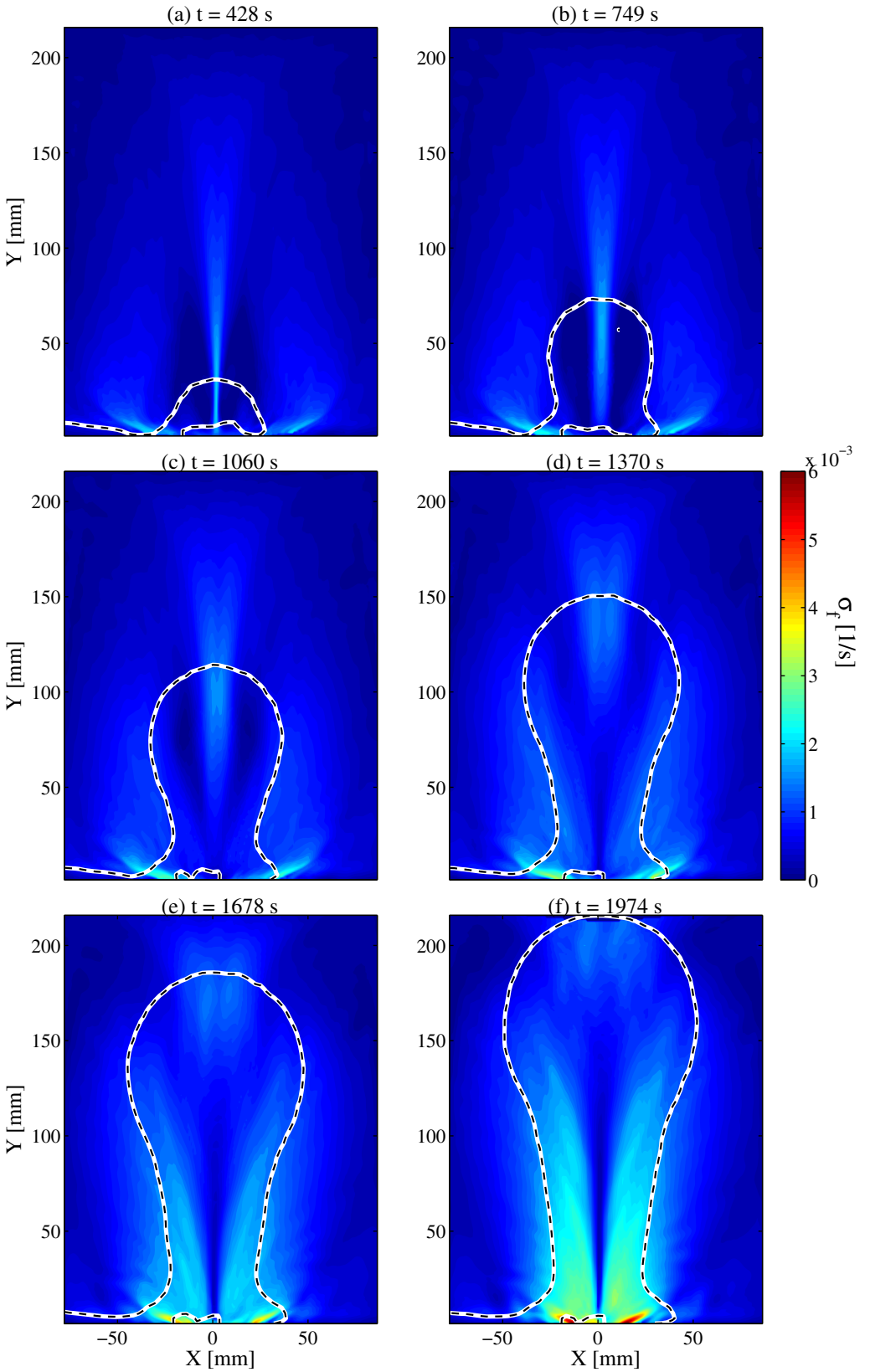

Figure 6. Contours of the Finite-Time Lyapunov Exponent field computed in forward-time, and the 25.25°C ($\Delta T = 0.05$°C) isotherm (white lines) measured at the center-plane ($z = 0$) at six instances for Ra = 1.37×10^6. In each case, the tracers were advected from the start of the experiment ($t = 0$) until the present time, t.

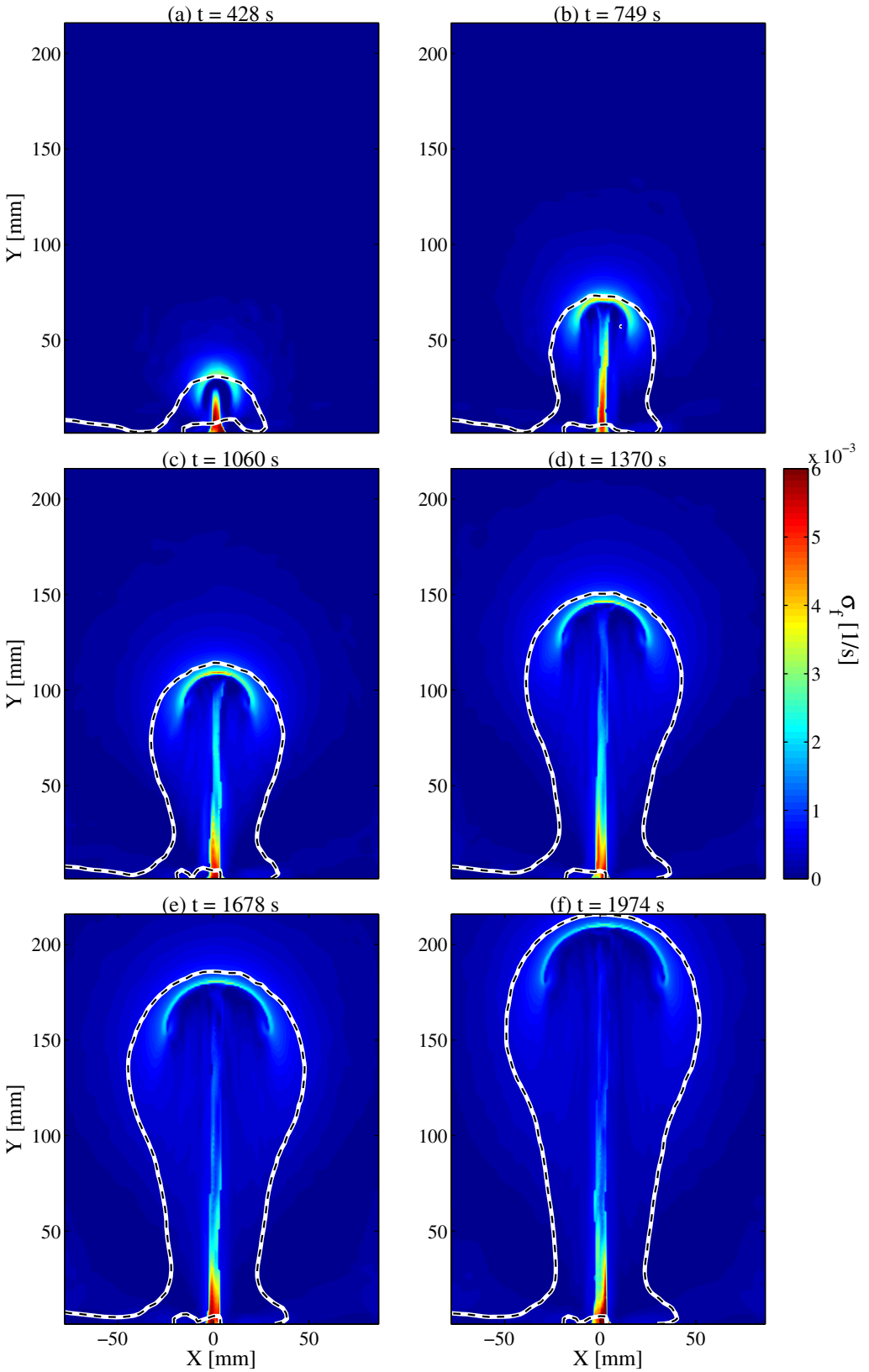

Figure 7. Contours of the Finite-Time Lyapunov Exponent field computed in backward-time, and the 25.25°C ($\Delta T = 0.05$°C) isotherm (white lines) measured at the center-plane ($z = 0$) at six instances for Ra = 1.37×10^6. In each case, the tracers were advected backward from the present time, t, until the start of the experiment ($t = 0$).

backward-time fields the inverse was true; tracers were advected in reversed flow from the current time until the start of the experiment. As it was not possible to measure the velocity fields throughout the entire test section (in particular close to the lower surface), some tracers advected out of the PIV domain. For these tracers, σ_f was calculated using the time at which they left the domain.

3. Results

3.1. Velocity Fields

The velocity fields measured in the center-plane of the test section are shown in Figure 5 at six instances throughout the $\mathrm{Ra} = 1.37 \times 10^6$ experiment. The contours represent the magnitude of the vertical velocity component, while the black lines show the 25.25°C isotherm ($\Delta T = 0.05$°C). This isotherm may be viewed as the boundary of the thermal anomaly of the plume. In all cases, the plume appears to contain small regions near the heater below 25.25°C (i.e., a smaller, closed isotherm is visible near $x = y = 0$); this is physically unrealistic and can be attributed to experimental error caused by the variations in the refractive index. Similarly, the isotherm indicates that the fluid is above 25.25°C along the lower left surface of each field. This is likely to be caused by errors associated with the reflections from the bottom of the tank.

As the heater is turned on at $t = 0$, the fluid heat is conducted radially outward, forming a circular dome of the hot fluid as can be seen in Figure 5a. At later times, this hot fluid begins to rise from the heater due to buoyancy forces, causing a contraction in the width of the 25.25°C isotherm near the heater (Figure 5b). This is the onset of the classical mushroom-like shape, containing a bulbous head and narrow stem, associated with plumes [*Griffiths and Campbell*, 1990]. This structure becomes more distinct as time progresses (Figures 5c–5f); the head of the isotherm surrounding the plume remains largely circular and increases in width as it rises, while near the heater, the stem gradually becomes narrower.

In most experimental studies of model plumes, it is typical to define the plume position using (direct or indirect) temperature measurements [*Moses et al.*, 1993; *Kaminski and Jaupart*, 2003] or velocity measurements/flow visualization [*Kumagai and Kurita*, 2000; *Griffiths and Campbell*, 1990] only. However, Figure 5 indicates that there are distinct differences between the velocity contours and the isotherm surrounding the plume, and measurements performed using either the temperature or the velocity field may not be consistent. For example, in all cases, there is significant vertical velocity above the highest point of the 25.25°C isotherm, indicating that this isoline does not delineate the boundary of the kinetic energy associated with the plume.

It is clear that the measurements of the velocity field in an Eulerian (i.e., lab-based) reference frame do not yield a simple means to identify the geometry or position of the thermal plume. It is often easier to identify convecting flow features such as the plume head in a reference frame which moves with the feature (i.e., a Lagrangian frame) [*O'Farrell and Dabiri*, 2010]. In the following section, the potential of Lagrangian analysis to provide information on the geometry of the plume is examined.

3.2. FTLE Fields

The forward and backward-time FTLE fields are shown in Figures 6 and 7, respectively, which correspond to the time steps shown in Figure 5. Throughout the development of the thermal plume, the forward-time fields presented in Figure 6 retain some basic features. For all six times, there appear two slightly inclined ridges on either side of the heater (starting at about $x \pm 10$ mm). The velocity fields in Figure 5 do not suggest that the ridges separate distinct regions of the flow, and show that there is significant flow normal to these ridges; therefore, these lines can be said to not represent material lines.

At early times (Figures 7a and 7b), a vertical ridge is apparent along the axis of symmetry ($x = 0$). This can be explained by considering two neighboring particles near the base of the plume, separated by a small distance (i.e., positioned at $x = \pm\delta_x$). As the plume develops, they will rise into the head and be convected to either side. However, at later times, they will not reach the top of the plume head within the integration time, τ, and they will not separate. Therefore, the ridge is not apparent near the heater at later times ($t \gtrsim 1060$ s).

The vertical ridge at $x = 0$ is also apparent in the backward-time FTLE fields (Figure 7), although in this case it remains attached to the heater at all times. Examination of the velocity fields in Figure 5 indicates that

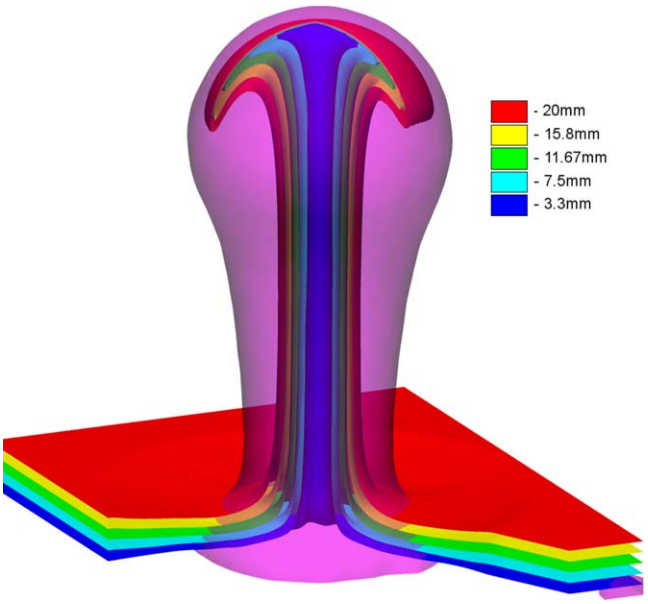

Figure 8. Three-dimensional view of the tracers used to compute the FTLE fields, for $t = 2217$ s and Ra $= 1.37 \times 10^6$. Over 6.3×10^6 tracers were convected using all 52 PIV planes. The opaque sheets represent the tracers which originated from different heights in the fluid domain, and the transparent shroud represents the 25.3°C isotherm. The corresponding two-dimensional velocity and FTLE fields are shown in Figures 5e, 6e, and 7e, respectively.

there is negligible flow perpendicular to this ridge in the forward and backward-time FTLE fields, and it can be said to represent a material line, or LCS, in the flow.

However, the character of the LCS varies along its length. In the backward-time FTLE field, the ridge is strongest near the heater. In this region, fluid particles are advected toward this line to feed the stem. However, in the forward-time fields, the ridge is apparent close to the plume head; in this case, particles along the ridge tend to advect *away* from the line, as they are drawn into the wider regions of the head. This implies that the material line along the plume stem is a *repelling* LCS near the heater, but an *attracting* LCS in the plume head.

Lastly, there is an arc-shaped ridge in the backward-time FTLE near the top of the isotherm. This marks part of the kinematic boundary at the top of the plume; elements below the arc-like ridge form the plume head, while those above it constitute ambient material. This ridge also marks a material line of the flow, which is consistent with the shadowgraph experiments of *Schlien* [1976], who found that ambient fluid only entered the plume head from the base of the cap, with none passing through the cap itself. This ridge is closely aligned with the top of the 25.25°C isotherm throughout the development of the plume (Figures 7a–7f, $t = 428$–1974 s), and represents a means by which the velocity fields can be used to measure the geometry of the thermal plume in a manner which is consistent with the temperature measurements. The isotherm tends to be slightly wider, which is likely to be due to the conduction of heat out of the plume head, rather than the convection of fluid (as will be shown in section 3.3).

The forward and backward-time FTLE fields together indicate that the regions of strongest fluid stretching occur along the plume axis and on the upper surface of the plume head. The broad regions of high σ_f at later times (Figure 6f) also indicate that there is significant stretching across the width of the 25.25°C isotherm for much of the height of the plume stem ($y \leq 140$ mm).

The convection of tracers and the FTLE field can also be computed in three dimensions, which can be used to visualize the full plume structure, as shown in Figure 8. The symmetrical nature of the thermal plume and the head and stem structure of the plume can clearly be seen, indicating that the LCSs discussed above are in fact three-dimensional features of the flow. A video showing the three-dimensional development of the thermal plume in terms of the backward-time σ_f field and $\Delta T = 0.05$°C isotherm is provided in the supporting information. Although useful in terms of visualizing the flow, such calculations involve the use of over 6.3×10^6 passive tracers, and therefore are associated with a significant computational cost. They were not found to provide an improved quantitative description of the plume dynamics compared to the FTLE field measured from the PIV fields acquired in the mid-plane of the test section, and therefore it was decided to perform the following analysis using only the two-dimensional FTLE fields.

3.3. Tracer Paths and Entrainment

Much of our understanding of mantle plumes is inferred from the isotopic signatures of lavas formed at hot spots [*Zindler and Hart*, 1986; *Hofmann*, 1997]. The interpretation of such data is ambiguous, as it is not clear where in the mantle the material observed at hot spots has originated from [*White*, 2010; *Hawkesworth and*

Scherstén, 2007]. Numerical and experimental models have the potential to help interpret the geochemical data from hot spot basalts if they can provide an indication of the origin of the material in the region where a plume nears the lithosphere (i.e., where partial melting is most likely to occur). Recent works by *Farnetani and Hofmann* [2010] and *Farnetani and Hofmann* [2013] have attempted to explain the isotopic variability observed in the Hawaiian hot spot by numerically modeling the flow of tracers beneath a moving plate and identifying the origin of the tracers that occupy the regions where melt is expected to occur.

In this section, we apply a similar approach to the experimental data, which provides a more general description of the behavior of isolated thermal plumes. Information on the origin of the fluid throughout the measurement domain is readily available from the Lagrangian analysis presented in the previous section. In order to compute the FTLE fields presented in Figure 7, over 379,000 passive tracers were numerically advected through the PIV domain in backward-time. The origin of each tracer at the moment when the plume reaches the top of the PIV domain can be identified by allowing the tracers to advect in backward-time from this point to the time when the heater was turned on. The tracer advection was implemented in the same manner described in section 2.3, except that here the spatial resolution was greater, 0.31×0.31 mm.

It should be noted that by analyzing the origin of the tracers at the instant at which the plume reaches the top of the PIV domain, rather than the point at which it reaches the top of the tank, we are neglecting any interference effects between the plume and the solid boundary—or in the case of the mantle, between the plume and the lithosphere. However, the case of mantle plume and lithosphere interaction is likely to be more complex than the ideal case of a plume arriving at a rigid, no-slip boundary (such as the surface of the tank) due to phenomena such as partial melting, the motion of the overriding plate and the intervening low-viscosity asthenosphere layer, and may be complicated by the effects of the potential variations in the fluid properties across the 410 and 660 km discontinuities. All these features are likely to have complex effects on the flow which are difficult to predict or model experimentally. Therefore, in the current discussion, we have chosen to ignore the interaction between the plume and the surface. Instead, we address the ideal case of a plume as is nears the surface, but remains a small distance away from it, and neglect the effects of any phase changes (as might occur at the various seismic discontinuities).

Figures 9a and 9b show the PIV domain at $t = 2089$ s, with the color indicating the vertical and horizontal origin of each fluid tracer. This field was found by advecting the tracers in backward-time, as outlined above. Some tracers advected out of the measurement domain (indicating that in forward-time they originated from outside the domain), which correspond to the white regions in Figure 9. Figure 9a shows that nearly all the material in the plume head originated from deep in the fluid ($y \leq 50$ mm), in agreement with the common interpretation of hot spot lavas as being representative of the bottom or base of the mantle layer from which they originated. Many of the tracers in the stem and the material near the axis ($x = 0$) have originated from outside the PIV domain, implying they came from the 1.39 mm gap between the bottom of the tank and the lowest PIV measurement.

While it is not possible to track the location from which these tracers advected, the area of the lower surface of the test section from which these tracers originated can be estimated using simple analysis. As can been seen in the supporting information video, the plume is axisymmetric. Therefore, the volume of the plume stem that is occupied by tracers from outside the PIV domain is given by

$$V_s = \frac{\pi \overline{d_s}^2 L_s}{4}, \tag{5}$$

where $L_s = 215.9$ mm is the height of the white region in Figure 9, and $\overline{d_s} = 6.3$ mm is its mean diameter (width). By approximating the mean horizontal velocity as uniform across the layer at the bottom of the test section ($y \leq 1.39$ mm), the volume from which this fluid originated is likewise given by

$$V_o = \frac{\pi d_o^2 L_o}{4}, \tag{6}$$

where $L_o = 1.39$ mm is the height and d_o is the diameter of the region at the bottom surface which fed the plume stem. Equating V_s and V_o, the diameter of the feeder region is given by

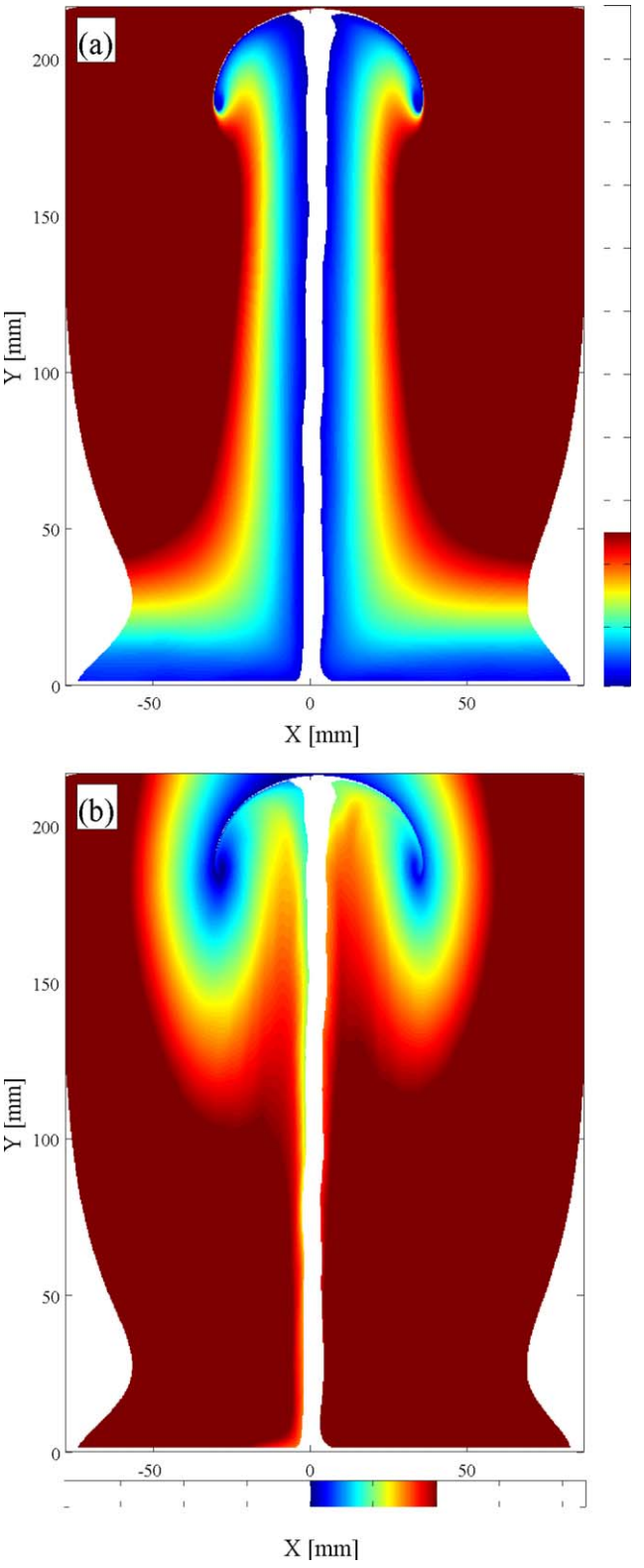

Figure 9. (a) Vertical and (b) horizontal origin of the tracers at $t = 2089$ s, for Ra $= 1.37 \times 10^6$. Over 40,000 uniformly distributed, passive tracers were numerically advected backward in time from $t = 2089$ s to the point at which the heater was turned on ($t = 0$), to ascertain where they originated from. White regions represent areas where the tracers originated outside the PIV domain.

$$d_o = \overline{d_s}\sqrt{\frac{L_s}{L_o}} = 78.52\ \text{mm}. \quad (7)$$

Figures 9 indicates that as the plume nears the surface, the stem has accumulated material from an area significantly larger than the area of the plume head, $d_o/d_h = 1.16$ (where $d_h = 67.8$ mm is the approximate diameter of the head, taken as the maximum width of material in the plume which has originated from $y \leq 50$ mm). The simple analysis presented here demonstrates the ability of thermal plumes originating from a point source to bring to the surface material from a wide area very close to the base of the fluid domain. For the case of a large mantle plume arising from the CMB, this implies that the material brought to the surface has originated over an area of the CMB far wider than that of the hot spot (as inferred from the area of active volcanism, the local geoid anomaly or tomography). However, it should be noted that in the case of the mantle, the simply scaling analysis used in equation (7) may become inaccurate as the plume begins to experience the effects of the presence of the lithosphere and the potential changes in viscosity and/or density at the transition between the upper and lower mantle [*Kumagai and Kurita*, 2000; *Kumagai et al*., 2007].

The large size of the source region and the comparatively small width of the stem indicate that mantle plumes may be effective at concentrating large-scale heterogeneities into a relatively small scale, which may explain the lateral variation in the isotopic signatures found in some OIBs. This is consistent with the earlier observation, based on the FTLE fields in Figures 6 and 7, that strong fluid stretching occurs along the entire length of the plume stem.

Abouchami et al. [2005] analyzed the temporal variability of the lead-

isotope signatures of the Hawaiian mantle plume (inferred from the depth of the samples acquired in the Hawaiian Scientific Drilling Project) and suggested that the isotopic variability has a length scale in the range 5–50 km (depending on the rise velocity of the plume). They also inferred that the isotopically distinct regions occurred as long, narrow vertical streaks in the plume stem. The simple analysis presented here indicates that the small-scale heterogeneity observed in the Hawaiian plume is likely to be influenced by the ability of the plume to sample a very wide region of the source material and compress it into a relatively narrow conduit, which will involve a reduction in the length scale of heterogeneity. This is in agreement with the numerical analysis performed by *Farnetani and Hofmann* [2010].

In the case of the mantle, the presence of a free-slip boundary condition at the lower surface (due to the very low viscosity of the liquid iron in the outer core relative to the mantle) and the reduced local viscosity in the mantle itself (due to the thermal effects of base heating and potentially also due to the presence of post-Perovskite, which is thought to have a lower and anisotropic viscosity [*Ammann et al.*, 2010]) may mean that mantle plumes sample from an even wider area of the CMB than Figure 9 suggests. Future work is planned to investigate the effects of base heating (compared to a point source) on the entrainment from the lower boundary layer.

Other than the plume stem, Figure 9b indicates that the plume has not entrained much material from the mid-depths of the fluid (i.e., $y \gtrsim 50$ mm). Here "entrainment" is taken as the incorporation of ambient material into the plume head by mechanical stirring, as described by *Griffiths and Campbell* [1990], rather than the heating of ambient material near the plume which then becomes viscously coupled to the plume [*Hauri et al.*, 1994]. Figure 9b shows that, other than the stem, all the material in the plume head has originated within 40 mm of the plume source. In general, the plume appears to bring material from the lower to the upper surface efficiently, but does not appear to significantly stir or mix the material lateral to the plume path (i.e., $|x| \gtrsim d_h/2$).

It is possible that the scrolls at the edges of the plume head (shown in detail in Figure 10) are capable of entraining ambient material more effectively, as suggested by *Griffiths and Campbell* [1990]. However, the resolution of the PIV measurements does not allow the scrolls to be fully resolved. The scrolls do not occupy a large area of the plume head in Figure 9, and therefore even if they do contain some unresolved entrained material, in the absence of significant additional entrainment at the 410 km or 660 km transitions (which are not modeled here), it is unlikely to be large enough to significantly alter the overall chemical composition of the plume head.

The black lines in Figure 10 represent the arc-like ridge of the FTLE fields computed in backward-time, which were presented in Figure 7. It is clear that the ridge in the FTLE field marks the boundary between the material above the plume originating deep in the fluid (blue) and that from the shallower depths (dark red). This again demonstrates that the FTLE is an effective means to find the material line surrounding the plume and identify the plume geometry, as suggested in section 3.2. It also confirms the observation regarding Figure 7 that the increased width of the isotherm in this region, relative to the width of the FTLE ridge, is caused by the conduction of heat rather than the advection of fluid, as it is clear that no fluid tracers from within the plume have advected beyond the FTLE ridge.

It is clear from the results presented here that the temperature and Lagrangian (FTLE and tracer fields) measurements reveal different aspects of the plume behavior and pose different advantages depending on the nature of the study. The temperature measurements reveal the thermal anomaly associated with the plume, and are useful in the analysis of heat transfer caused by plumes and their potential to produce partial melting in the mantle. However, they do not provide information on the transport of material within the flow and, as discussed in the previous paragraph, on their own they cannot distinguish between material that has risen due to convection and material surrounding the plume head that has gained heat by conduction. In contrast, the Lagrangian analysis is beneficial in the study of the dynamics, mixing and entrainment associated with plumes. The FTLE ridges reveal not simply the plume position, but also the shape of the plume head, the regions of strongest stretching and provide a clear means of separating the material in the rising plume head from the ambient material. Lagrangian analysis therefore represents a valuable tool when investigating the dynamics of plumes in the laboratory and the mantle.

3.4. Rise Velocity of Plumes

If a mantle plume has a low rise velocity, the buoyant material rising from the deep mantle will have a greater amount of time to cool and is less likely to cause decompression melting. Such a plume will affect

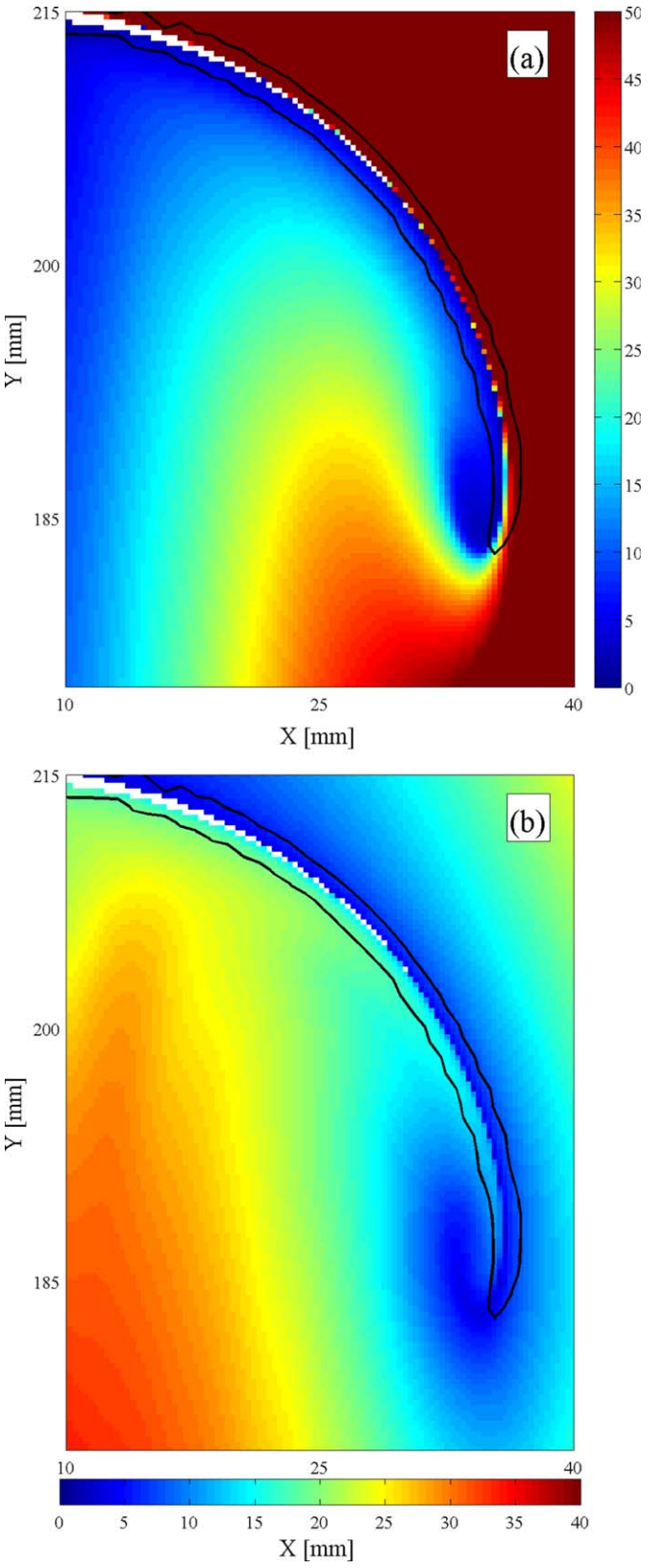

Figure 10. (a) Vertical and (b) horizontal origin of the tracers at $t = 2089$, showing the scroll region of the plume. The colors are defined in the same manner as Figure 9. The black line is an isoline where the FTLE fields computed in backward-time is greater than $1.5\times10^{-3}s^{-1}$.

the local geoid due to its low relative density, but is less likely to cause significant melting and volcanic activity at the surface. In contrast, a fast-rising plume will bring anomalously hot material to the surface significantly faster than it can cool and is more likely to result in the formation of a large igneous province when it reaches the surface. While the size of the plume (i.e., the volume of buoyant material rising) is likely to have a strong effect on the magnitude of the volcanic activity, it is clear that the rise velocity has a crucial role in determining whether a mantle plume is capable of inducing melting and volcanism. The rise velocity of plumes is also important for the study of the rate at which chemical heterogeneities are transported through the mantle and the nature of heat transport away from the core. Therefore, it is of great interest to gain a deeper understanding of how the rise velocity scales with various fluid and experimental parameters, as will be discussed in this section.

The location of the maximum of the backward-time FTLE field in the ridge marking the upper edge of the plume head can be used to define the plume position. This approach was found to be consistent with the estimation of the plume height from the maximum in the horizontal velocity gradient, $\partial u/\partial x$ in Cartesian coordinates [*Davaille et al.*, 2011] but contained less noise. The variation in the plume position as a function of time is shown in Figure 11 for each of the four experiments. In each case, the plume begins to rise slowly before entering a steady state stage in which the plume height has an approximately linear dependence on time, as indicated by the closed symbols.

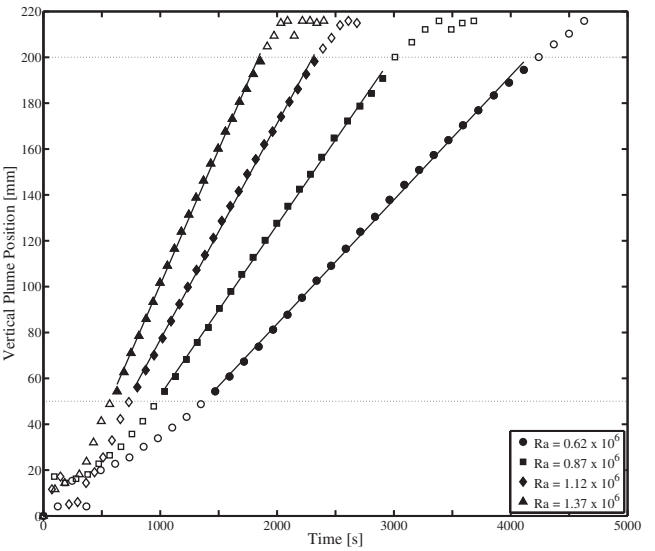

Figure 11. Variation in the position of the plume head with time for four ΔT experiments. The closed symbols indicate the points which were used to calculate the rise velocity for each case.

When the plume height exceeds $y \approx 200$ mm (dashed line in Figure 11), the top of the head nears the upper boundary of the PIV domain (and the FTLE field), and the values of the plume height are no longer representative of the true position, and can be ignored. Similarly, when the plume height is less than approximately 50 mm, the plume has not yet reached a steady state, and the data points for $y \leq 50$ mm can also be ignored.

This period of constant rise velocity was also observed in the flow visualizations of *Kaminski and Jaupart* [2003] for various fluids spanning a range of Prandtl numbers, as well as *Schlien* [1976] and *Coulliette and Loper* [1995], amongst others. In contrast, *Whittaker and Lister* [2008] showed that the height of a thermal (i.e., a volume of buoyant fluid released at $t = 0$, with no continued supply of heat) will increase as $\sim t^{1/2}$. In the latter case, the decrease in the rate of the rise velocity of the thermal is due to the thermal diffusion and fluid entrainment. It appears that the presence of heat source in the case of a thermal plume provides the plume with sufficient energy to overcome these effects and allows the system to reach a steady state where the height scales as $\sim t$.

The steady state rise velocity, U_r, of each of the four experiments was found by fitting a linear regression to the closed symbols in Figure 11, and the variation with ΔT is shown in Figure 12a. The uncertainty in the calculation of U_r was taken to be the same as the maximum error in the PIV estimates along the plume axis (6.3%). It is apparent that the rise velocity follows a linear relationship with the applied temperature difference. In order to generalize these results and extrapolate them to conditions relevant to the mantle, it is necessary to nondimensionalize the parameters. The temperature difference is normalized as the Rayleigh number, while the rise velocity is presented in the form of the Péclet number, $\mathrm{Pe} = U_r d_h / \kappa$, which is the ratio of the rate of heat transport due to convection and that due to conduction. The diameter of the plume, d_h, is found using the definition presented in the previous section (i.e., the maximum width of tracers originating from $y \leq 50$ mm in the plume as it reaches the top of the PIV domain). The relationship between Pe and Ra can be expressed as

$$\mathrm{Pe} = 3.82 \times 10^{-5} \mathrm{Ra} + 24.3, \tag{8}$$

as shown in Figure 12b. Below the critical Rayleigh number, which is typically of the order $\mathrm{Ra}_c \sim 10^3$, no plumes will form and neither d_h nor Pe can be defined. Therefore, Ra_c can be said to represent a discontinuity in equation (8) and the relation will not be valid at lower Rayleigh numbers. This explains the apparent prediction that a finite rise velocity will exist for the case $\Delta T \leq 0$.

Assuming the mantle to have a Rayleigh number and thermal diffusivity of 10^7 and $10^{-6} \mathrm{m}^2/\mathrm{s}$, respectively, equation (8) predicts that a plume head with a diameter of 1000 km (the size estimated by *Campbell* [2005]) will have a rise velocity of 12.8 mm/a. This implies that a plume of this scale would take approximately 218 Ma to rise from the CMB to the lithosphere (taken here as 100 km depth), which is of the same order of magnitude as *Campbell*'s [2005] prediction of 100 Ma (based on scaling arguments). It also has the same order of magnitude as the estimates noted by *White* [2010] (based on a range of geochemical data), whereby a plume is expected to have a rise velocity in the range 20–60 mm/a. This would indicate that the values predicted by equation (8) are reasonable. However, such estimates should be treated with caution

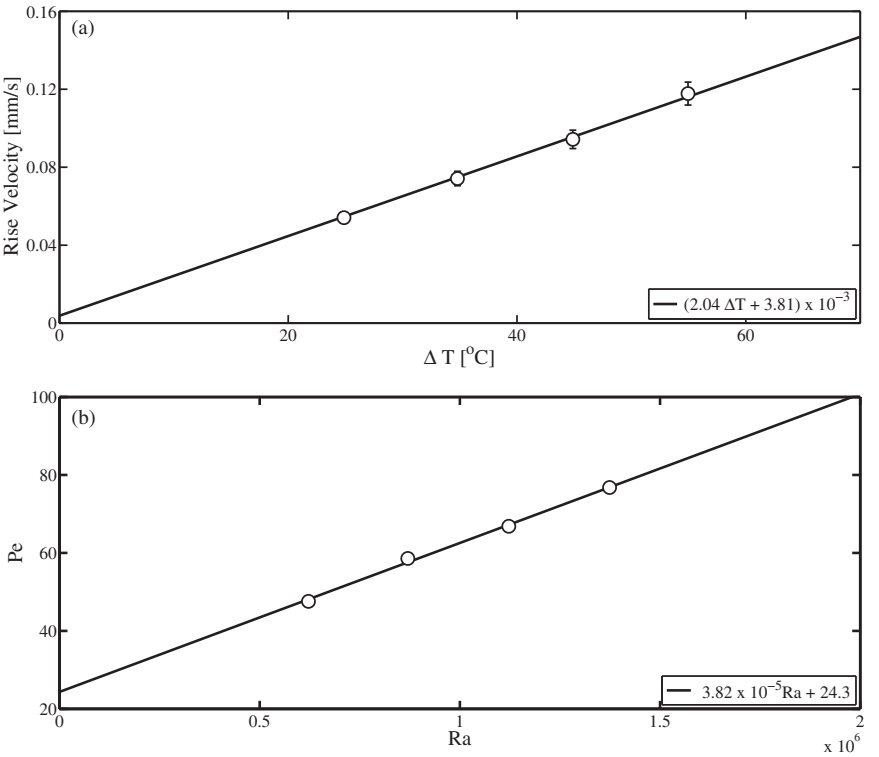

Figure 12. (a) Variation in the rise velocity of the plume with the applied ΔT, and (b) the variation in the Péclet number with the Rayleigh number. The velocities for each case were found by fitting a linear regression to the closed points in Figure 11.

for a number of reasons, in particular in relation to the effects of the Prandtl number, and the choice of the nondimensional parameters.

The asymptotic analysis of *Worster* [1986] indicates that the rise velocity should scale as

$$U_r \propto \left(\log \varepsilon^{-2}\right)^{1/2}, \tag{9}$$

where ε is a solution of $\varepsilon^4 \log \varepsilon^{-2} = 1/\mathrm{Pr}$ (for $\mathrm{Pr} > 7$), which was in agreement with the experiments of *Kaminski and Jaupart* [2003]. Assuming the mantle to have a Prandtl number of 10^{23} (and recalling that for the syrup, $\mathrm{Pr} = 2.1 \times 10^5$) the true rise velocity of a mantle plume will be larger than the value predicted by equation (8) by a factor of 1.99. Taking this into account, the rise velocity of the mantle plumes predicted by equation (8) now becomes 25.5 mm/a, with a rise time of 109 Ma, which are in close agreement with the estimates of *White* [2010] and *Campbell* [2005].

This factor, 1.99, is actually rather small, especially when viewed in the context of the large uncertainty in the various parameters of the mantle (κ, ν, etc.) and the plume diameter, and serves as a reminder of the potential of lab-scale experiments to model the behavior of the mantle despite the vast differences in fluid properties and time scales involved.

A second and more significant limitation arises from the use of only one fluid in the experiments; this means that the various fluid parameters involved in the nondimensionalization (κ, ρ, ν, etc.) remain constant and it remains uncertain whether the nondimensional numbers employed here are appropriate. For example, the rise velocity could equally be expressed as the Reynolds number, $\mathrm{Re} = U_r d_h / \nu$ instead of Pe.

The characteristic length with which the rise velocity scales has significant implications for mantle dynamics. *Moses et al.* [1993] nondimensionalized the rise velocity using κ and the width of the heater element, R_0 (i.e., $\mathrm{Pe} = U_r R_0 / \kappa$). It is not clear how this would be applied to mantle conditions where plumes do not originate at fixed sources of finite width, but arise due to plate-heating at the core-mantle boundary (or the 660 km discontinuity).

Table 2. Details of various previous theoretical and experimental studies which examine the rise velocity of plumes and are discussed in section 3.4

Study	Buoyancy Source	Viscosity Contrast	Notes
Batchelor [1954]	Point source	$\gamma = 1$	Unbounded fluid domain
Whitehead and Luther [1975]	Rayleigh-Taylor flow	Variable γ	No heating system
Olson and Singer [1985]	Injection of hot fluid	$\gamma \approx 1$	
Griffiths and Campbell [1990]	Injection of hot fluid	$\gamma \approx 333$	
Moses et al. [1993]	Heater	Not reported	
Kaminski and Jaupart [2003]	Heater	$\gamma < 2$	

The Péclet number could equally be defined in terms of the diameter of the stem or the depth of the fluid domain (the characteristic length in Ra), rather than d_h. The choice of these definitions would have a significant effect on the value of the rise velocity predicted to occur in the mantle, and highlights the importance of identifying the nondimensional parameters relevant to mantle convection, in particular the length and time scales governing the rise velocity.

It is also significant that the data in Figure 12 clearly indicate that the rise velocity is linearly dependent on Ra, which is in contrast to the findings of previous studies. Details of various previous studies in the literature which are discussed in this section are summarized in Table 2. The scaling laws presented by *Batchelor* [1954] indicate that the rise velocity should scale as

$$U_r \propto \left(\frac{g\alpha Q}{\rho \nu C_p}\right)^{1/2}. \tag{10}$$

where Q is the power output of the heat source. This can also be expressed as in terms of Ra_Q as,

$$U_r \propto \mathrm{Ra}_Q^{1/2}\kappa, \tag{11}$$

which suggests a square-root dependence on the Rayleigh number. The experimental measurements of *Kaminski and Jaupart* [2003] were in good agreement with equation (10), and they found that $U_r \propto Q^{1/2}$. However, the fluids they examined did not have a wide range of thermal diffusivity ($\kappa = 0.06-0.14\,\mathrm{mm}^2/\mathrm{s}$), and they did not express their data in the form of equation (11) explicitly.

Moses et al. [1993] found a similar relation (in their Figure 4),

$$U_r \propto \frac{\kappa}{R_0}\left(\frac{\mathrm{Ra}_Q}{\mathrm{Pr}}\right)^{1/2} = R_0\left(\frac{\mathrm{Ra}_Q}{\kappa\nu}\right)^{1/2}. \tag{12}$$

In contrast, *Griffiths and Campbell* [1990] assumed the thermal plume can be described as a buoyant Stokes sphere, with temperature-dependent viscosity such that the viscosity of the hot fluid was much smaller than that of the ambient fluid, and showed that

$$U_r \propto \mathrm{Ra}\left(\frac{d}{D}\right)^2, \tag{13}$$

where d is the width of the plume (or the Stokes sphere, in their analysis). For the rise velocity to scale with $\mathrm{Ra}^{1/2}$, this would require that $(d_h/D) \propto \mathrm{Ra}^{-1/4}$. Although d_h was found to decrease slightly with Ra, this scaling relation was not observed in the current work.

It is clear that the exact scaling between the rise velocity of a thermal plume remains uncertain and lacks definitive experimental verification. In particular, the dependence of the velocity on the Rayleigh number and κ remains ambiguous.

It is possible that this apparent inconsistency is due to the different forms of the Rayleigh numbers used in the study of *Kaminski and Jaupart* [2003] and *Moses et al.* [1993] (i.e., Ra_Q instead of Ra). However, this would imply that the temperature output of the heater used in their experiments scaled with the square root of the input power, which is physically unrealistic. The $U_r-\mathrm{Ra}$ relation may also be influenced by the finite size of the fluid domain in the current study; *Batchelor* [1954] was primarily concerned with plumes in air, and therefore when deriving the plume scaling relations he assumed a fluid domain which was unbounded. *van*

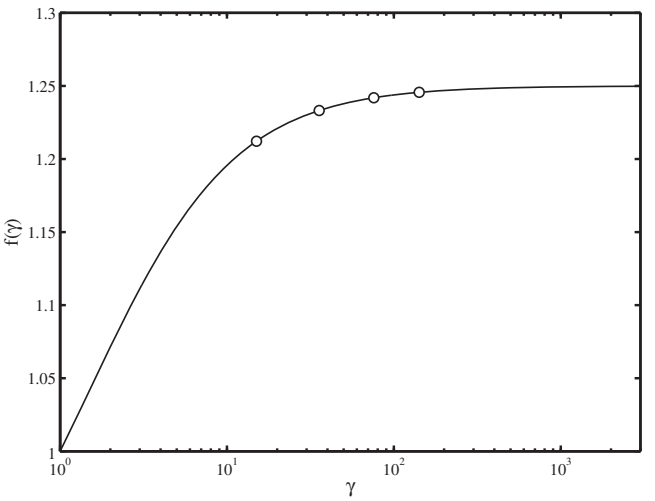

Figure 13. Variation in the scaling factor of the rise velocity of buoyant Stokes sphere rising through ambient fluid. The black line represents equation (14), while the symbols corresponds to the experiments performed here, with the temperature contrast taken at the difference between the heater and the ambient temperatures. A fluid with isoviscous properties corresponds to $\gamma = 10^0$.

Keken et al. [2013] performed a series of numerical simulations in which the size of the fluid domain and the boundary conditions at the top surface were varied, and showed that the vertical velocity along the steady state plume axis differed from the theoretical predictions if no fluid was allowed to pass through the upper surface of the simulation domain (i.e., the fluid was in a "closed box"). However, it is not clear what effect this would have on the Rayleigh number dependence of U_r.

Alternatively, the cause of this disagreement may also be related to the temperature dependence of the viscosity in the current experiments. *Batchelor* [1954] assumed a viscosity which did not vary with depth or temperature, while the various fluids employed in the experiments of *Kaminski and Jaupart* [2003] were chosen to minimize the variation in viscosity with temperature. They state that the largest change in viscosity encountered away from the heater in their experiments was less than a factor of 2, whereas equation (3) suggests a significantly larger variation in the viscosity in the current set of experiments.

Olson and Singer [1985] used flow visualization to examine the growth of plumes which were generated by injecting buoyant fluid into a tank. In their experiments, the buoyancy was induced by compositional changes (diluting sugar syrup with water) rather than temperature changes, which allowed them to study the case in which the viscosity in the plume was approximately equal to the ambient fluid, and in which the plume viscosity was much lower. In the former case, the plume stem was wide, the head was small and the rise velocity scaled as that of a vertical cylinder rising (i.e., the rise velocity was controlled by the viscous stresses acting along the stem rather than the head). In the latter case (which is analogous to a thermal plume in a fluid with a highly temperature-dependent viscosity), the plume had a very narrow stem and a wide, well-defined spherical head (see Figure 3 in *Olson and Singer* [1985] for a comparison). A similar effect can be seen in the flow visualization of Rayleigh-Taylor instability by *Whitehead and Luther* [1975]. The case of the variable viscosity plume is far more likely to resemble the ideal case of a Stokes sphere, and therefore to follow the linear scaling relationship with the Rayleigh number (as predicted by equation (13) and seen in Figure 12). It should be noted however, that in the experiments of Olson and Singer, the rise velocity was not constant, which is likely to be a consequence of the fact that their plumes were generated by injected material rather than a heat source, as in the current work and that of *Kaminski and Jaupart* [2003] and *Moses et al*. [1993].

It is useful here to examine the case of a buoyant droplet of fluid, with an internal viscosity, $\mu_h = \mu/\gamma$, rising through ambient fluid. This is analogous to the hot plume head in the current experiments, where μ_h is given by equation (3). The variation in the viscosity causes the rise velocity to increase by a factor

$$f(\gamma) = \frac{5}{4}\left(\frac{\gamma+1}{\gamma+3/2}\right), \tag{14}$$

relative to the isoviscous case [*Batchelor*, 1954; *Davaille et al*., 2011]. In the current work, the viscosity contrasts were very large, and the magnitude of $f(\gamma)$ were quite uniform, occurring in the range 1.21–1.25, as shown in Figure 13. Apparently, for $\gamma \gtrsim 20$ the effects of the viscosity variations are relatively constant. However, below this value, γ has a significant effect on the rise velocity. The viscosity variations are controlled by the applied ΔT; therefore, they will depend on Ra, and are likely to affect the scaling relationship

between Ra and U_r when $\gamma \lesssim 20$. In practice, the plume head will be considerably colder than the heater temperature, and γ is likely to be lower than that shown in Figure 13. Without quantifiable temperature measurements in the plume head, it is difficult to estimate the true value of γ and the effect of the temperature-dependent viscosity on the rise velocity. However, the results discussed here demonstrate that the temperature-dependence of the fluid viscosity may play a significant role in determining the scaling laws of the rise velocity of thermal plumes, which has not received significant attention to date.

To fully address the question of how the behavior of the plumes in the mantle scales with the various mantle properties and boundary conditions requires further experiments using different fluids (e.g., isoviscous and fluids with strongly temperature-dependent viscosity) and methods of heat input (i.e., constant heater power and constant heater temperature, such that both forms of the Rayleigh number can be varied independently). It is also difficult to identify the role of the Prandtl number in the scaling relationships, and to confirm the appropriateness of the Péclet number as a means of nondimensionalizing the rise velocity, without investigating the behavior of plumes in a series of fluids spanning a wide range of Pr.

4. Conclusions

Three-dimensional measurements were presented of the velocity and temperature fields associated with a laminar, axisymmetric plume rising through a fluid with temperature-dependent viscosity. The velocity fields and the $\Delta T = 0.05^{\circ}$C isotherm measured in the symmetry plane were examined but were not found to present a reliable or consistent means of identifying the plume geometry. However, the FTLE fields computed in backward-time were shown to clearly identify the material line corresponding to the top of the plume head. This line marked the boundary between the ambient fluid and fluid which originated very close to the bottom surface of the test section, and provided an effective means of quantifying the plume position.

Examination of the paths of the fluid elements reveals that the thermal plume did not entrain significant material from the ambient fluid, as has previously been suggested [*Griffiths and Campbell*, 1990]. The plume stem was found to be composed of fluid which originated from a wide area very deep in the fluid domain, suggesting that the material contained in plume has undergone significant fluid stretching, which will act to reduce the length scale to heterogeneity. This is a possible contributing factor to the small-scale variability observed in some OIBs.

Lastly, the backward-time FTLE fields were used to estimate the position and rise velocity of the plume for a range of Rayleigh number. After an initial growth period, the plume reached a steady state phase in which the rise velocity was constant. This velocity was found to scale linearly with Ra, in contrast to the scaling relations predicted by *Batchelor* [1954] and the experimental evidence of *Moses et al.* [1993] and *Kaminski and Jaupart* [2003]. The importance of understanding the factors controlling the rise velocity was discussed and it was suggested that the differences in the scaling laws found in the current and previous studies may be attributed to the temperature-dependent viscosity of the fluid employed here.

Acknowledgments
We would like to thank two anonymous reviewers for their constructive comments and suggestions, and the Editor, Thorsten Becker, for his handling of the paper. This work was funded by the National Science Foundation (grant EAR-055199) and the MAPS Dean's Office at UCL.Please contact the corresponding author (neil.cagney.11@ucl.ac.uk) regarding any queries or requests relating to the data used in this work.

References

Abouchami, W., A. W. Hofmann, S. J. G. Galer, F. A. Frey, J. Eisele, and M. Feigenson (2005), Lead isotopes reveal bilateral asymmetry and vertical continuity in the Hawaiian mantle plume, *Nature*, *434*, 851–856.
Adrian, R. J., and J. Westerweel (2011), *Particle Image Velocimetry*, 1st ed., Cambridge Univ. Press. Cambridge, U. K.
Ammann, M. W., J. P. Brodholt, J. Wookey, and D. P. Dobson (2010), First-principles constraints on diffusion in lower-mantle minerals and a weak D'' layer, *Nature*, *465*, 462–465.
Barnea, D. I., and H. F. Silverman (1972), A class of algorithms for fast digital image registration, *IEEE Trans. Comput.*, *C-21*(2), 179–186.
Batchelor, G. K. (1954), Heat convection and buoyancy effects in fluids, *Q. J. R. Meteorol. Soc.*, *80*, 339–354.
Bercovici, D., and J. Mahoney (1994), Double flood basalts and plume head separation at the 660-kilometer discontinuity, *Science*, *266*, 1367–1369.
Campbell, I. H. (2005), Large igneous provinces and the mantle plume hypothesis, *Elements*, *1*, 265–269.
Campbell, I. H., and R. W. Griffiths (1990), Implications of mantle plume structure for the evolution of flood basalts, *Earth Planet. Sci. Lett.*, *99*, 79–93.
Chay, A., and D. J. Schlien (1986), Scalar field measurements of a laminar starting plume cap using digital processing of interferograms, *Phys. Fluids*, *29*, 2358–2366.
Coulliette, D. L., and D. E. Loper (1995), Experimental, numerical and analytical models of mantle starting plumes, *Phys. Earth Planet. Inter.*, *92*(3), 143–167.
Cowen, E. A., and S. G. Monismith (1997), A hybrid digital particle tracking velocimetry technique, *Exp. Fluids*, *22*, 199–211.
Cserepes, L., and D. A. Yuen (2000), On the possiblity of a second type of mantle plume, *Earth Planet. Sci. Lett.*, *183*, 61–71.

Dabiri, D. (2009), Digital particle image thermometry/velocimetry: A review, *Exp. Fluids*, *46*, 191–241.
Davaille, A., E. Stutzmann, G. Silveira, J. Besse, and V. Courtillot (2005), Convection patterns under the Indo-Atlantic "box", *Earth Planet. Sci. Lett.*, *239*, 233–252.
Davaille, A., A. Limare, F. Touitou, I. Kumagai, and J. Vatteville (2011), Anatomy of a laminar starting thermal plume at high Prandtl number, *Exp. Fluids*, *50*, 285–300.
Farnetani, C. G. and A. W. Hofmann (2010), Dynamics and internal structure of the Hawaiian plume, *Earth Planet. Sci. Lett.*, *295*, 231–240.
Farnetani, C. G. and A. W. Hofmann (2013), Two views of the Hawaiian plume structure, *Geochem. Geophys. Geosyst.*, *14*, 5308–5322, doi: 10.1002/2013GC004942.
Farnetani, C. G., and M. A. Richards (1995), Thermal entrainment and melting in mantle plumes, *Earth Planet. Sci. Lett.*, *136*, 251–267.
Farnetani, C. G., and H. Samuel (2005), Beyond the thermal plume paradigm, *Geophys. Res. Lett.*, *32*, L07311, doi:10.1029/2005GL022360.
Farnetani, C. G., E. Legras, and P. J. Teckley (2002), Mixing and deformations in mantle plumes, *Earth Planet. Sci. Lett.*, *196*, 1–15.
Fergason, J. L. (1968), Liquid crystals in nondestructive test, *Appl. Opt.*, *7*(9), 1729–1737.
Ferziger, J. H. (1998), *Numerical Method for Engineering Applications*, 2nd ed., Wiley & Sons, London, U. K.
Griffiths, R. W., and I. H. Campbell (1990), Stirring and structure in mantle starting plumes, *Earth Planet. Sci. Lett.*, *99*, 66–78.
Haller, G. (2015), Lagrangian coherent structures, *Annu. Rev. Fluid Mech.*, *47*, 137–161.
Hart, S. R., E. H. Hauri, L. A. Oschmann and J. A. Whitehead (1992), Mantle plumes and entrainment: Isotopic evidence, *Science*, *256*, 517–520.
Hauri, E. H., J. A. Whitehead, and S. R. Hart (1994), Fluid dynamic and geochemical aspects of entrainment in mantle plumes, *J. Geophys. Res.*, *99*(B12), 24,275–24,300.
Hawkesworth, C., and A. Scherstén (2007), Mantle plumes and geochemistry, *Chem. Geol.*, *241*, 319–331.
Hofmann, A. W. (1997), Mantle geochemistry: The message from oceanic volcanism, *Nature*, *385*(16), 219–229.
Kaminski, E., and C. Jaupart (2003), Laminar starting plumes in high-Prandtl-number fluids, *J. Fluid Mech.*, *478*, 287–298.
Kumagai, I., and K. Kurita (2000), On the fate of mantle plumes at density interfaces, *Earth Planet. Sci. Lett.*, *179*, 63–71.
Kumagai, I., A. Davaille, and K. Kurita (2007), On the fate of thermally buoyant mantle plumes at density interfaces, *Earth Planet. Sci. Lett.*, *254*, 180–193.
Li, M., A. K. McNamara, and E. J. Garnero (2014), Chemical complexity of hotspots caused by cycling oceanic crust through mantle reservoirs, *Nat. Geosci.*, *7*, 366–370.
Limare, A., I. Kumagai, J. Vatteville, and A. Davaille (2008), Thermal plumes visualization: Differential interferometery versus thermochromic liquid crystals, paper presented at the 13th International Symposium of Flow Visualization. University of Franche-Comté, Nice, France.
Lin, S.-C., and P. E. van Keken (2006), Deformation, stirring and material transport in thermochemical plumes, *Geophys. Res. Lett.*, *33*, L20306, doi:10.1029/2006GL027037.
Mathur, M., G. Haller, T. Peacock, J. E. Ruppert-Felsot, and H. L. Swinney (2007), Uncovering the Lagrangian skelton of turbulence, *Phys. Rev. Lett.*, *98*(144502), 1–4.
Morgan, W. J. (1971), Convective plumes in the lower mantle, *Nature*, *230*, 42–43.
Moses, E., G. Zocchi, and A. Libchaber (1993), An experimental study of laminar plumes, *J. Fluid Mech.*, *251*, 581–601.
Newsome, W. H. (2011), Experimental investigation of mass transport, dynamics, and stirring in isolated thermal plumes, PhD thesis, Univ. of Mich, Ann Arbor.
Nguyen, C. V., T. D. Nguyen, J. C. Wells, and A. Nakayama (2010), Interfacial PIV to resolve flows in the vicinity of curved surfaces, *Exp. Fluids*, *48*, 577–587.
O'Farrell, C., and J. O. Dabiri (2010), A Lagrangian approach to identifying vortex pinch-off, *Chaos*, *20*, 017513.
Olson, P., and H. Singer (1985), Creeping plumes, *J. Fluid Mech.*, *158*, 511–531.
Raffel, M., C. Willert, S. Wereley, and J. Kompenhans (2007), *Particle Image Velocimetry*, 2nd ed., Springer. New York, USA.
Raynes, E. P. (1983), Electro-optic and thermo-optic effects in liquid crystals, *Philos. Trans. R. Soc. London A*, *309*(1507), 167–178.
Rogers, M. C., and S. W. Morris (1990), Natural versus forced convection in laminar starting plumes, *Phys. Fluids*, *21*(083601), 1–7.
Schlien, D. J. (1976), Some laminar thermal and plume experiments, *Phys. Fluids*, *19*(8), 1089–1098.
Shadden, S. C., F. Lekien, and J. E. Marsden (2005), Definition and properties of Lagrangian coherent structures from finite-time Lyapunov exponents in two-dimensional aperiodic flows, *Physica D*, *212*, 271–304.
van Keken, P. (1997), Evolution of starting mantle plumes: A comparison between numerical and laboratory models, *Earth Planet. Sci. Lett.*, *148*, 1–11.
van Keken, P. E., A. Davaille, and J. Vatteville (2013), Dynamics of a laminar plume in a cavity: The influence of boundaries on the steady-state stem structure, *Geochem. Geophys. Geosyst.*, *14*, 157–178, doi:10.1029/2012GC004383.
Vatteville, J., P. E. van Keken, A. Limare, and A. Davaille (2009), Starting laminar plumes: Comparison of laboratory and numerical modeling, *Geochem. Geophys. Geosyst.*, *10*, Q12013, doi:10.1029/2009GC002739.
Westerweel, J., and F. Scarano (2005), Universal outlier detection for PIV data, *Exp. Fluids*, *39*, 1096–1100.
Westerweel, J., G. E. Elsinga, and R. J. Adrian (2013), Particle image velocimetry for complex and turbulent flows, *Annu. Rev. Fluid Mech.*, *45*, 409–436.
White, W. M. (2010), Oceanic island basalts and mantle plumes: The geochemical perspective, *Annu. Rev. Earth Planet. Sci.*, *38*, 133–160.
Whitehead, J. A., and D. S. Luther (1975), Dynamics of laboratory diapir and plume models, *J. Geophys. Res.*, *80*(5), 705–717.
Whittaker, R. J., and J. R. Lister (2008), The self-similar rise of a buoyant thermal in very viscous flow, *J. Fluid Mech.*, *606*, 295–324.
Willert, C. (1997), Stereoscopic digital particle image velocimetry for application in wind tunnel flows, *Meas. Sci. Technol.*, *8*, 1465–1479.
Worster, M. G. (1986), The axisymmetric laminar plume: Asymptotic solutions for large Prandtl numbers, *Stud. Appl. Math.*, *75*, 139–152.
Zindler, A., and S. Hart (1986), Chemical geodynamics, *Annu. Rev. Earth Planet. Sci.*, *14*, 493–571.